Caspase mediated beclin-1 dependent autophagy tuning activity and apoptosis promotion by surface modified hausmannite nanoparticle

Souvik Mondal[ab], Anupam Giri[c], Yunjiao Zhang[ab], Samir Kumar Pal[d], Wei Zhou[ab]* and Long-ping Wen[ab]*

[a] The CAS Key Laboratory of Innate Immunity and Chronic Disease, Innovation Center for Cell Signaling Network, School of Life Sciences and Medical Center, University of Science and Technology of China, Hefei, Anhui 230027, China

[b] Hefei National Laboratory for Physical Sciences at Microscale, University of Science and Technology of China, Hefei, Anhui 230027, China

[c] Department of Materials Science and Engineering, Pohang University of Science and Technology (POSTECH), 77 Cheongam-Ro, Nam-Gu, Pohang, Gyeongbuk, Korea 790-784;

[d] Department of Chemical, Biological & Macromolecular Sciences, S. N. Bose National Centre for Basic Sciences, Block JD, Sector III, Salt Lake, Kolkata 700 098, India

* Correspondence to: Long-ping Wen; Email: lpwen@ustc.edu.cn

Wei Zhou; Email: zhouweid@ustc.edu.cn

Abstract

Hidden effects of nano-materials to induced autophagy, a lysosomal degradative pathway, remain an exciting topic, in the level of material-protein interaction and subsequent cellular signaling features. Here, our studies show that surface modified hausmannite nanoparticles (Mn_3O_4 NPs) can uniformly cleave/splice Beclin-1 protein and alter cellular mechanism on the emphasis of tuning autophagy and subsequently promote enhancement of apoptosis. Details investigation of Beclin-1 dependency and its uniform cleavage/splice pattern by surface modified Mn_3O_4 NPs, shows tuning of cellular mechanism on emphasis of caspase mediated autophagy tuning. Our findings will also clarify the conflict between apoptosis-autophagy on the basis of its unique property derived from surface chemistry modulation, in context of Beclin-1 eminent cleavage/splice which remarks novel effect of Beclin-1 dependent tuning of autophagosomes formation and switch to enhance apoptotic index, mediates by PI3KC3 cleavage & caspase activation.

1. Introduction

The role of autophagy, a lysosomal degradative pathway, and its regulation in cancer cells continues to emerge, and several studies have aimed to define the optimal strategies to modulate autophagy for therapeutic advantages. This intracellular bulk degradation process mediates the clearance of long-lived proteins and damaged organelles by autophagosomes, the fusion of autophagosomes with lysosomes to form autolysosomes, and the subsequent degradation of the engulfed cytoplasmic contents by lysosomal enzymes.[1] Recent evidences support a relationship between several classes of nanomaterials and autophagy perturbation, both induction and blockade, in many biological models, causes mainly due to the dynamic nature of the physicochemical interactions at the 'nano-bio' interface that comprises kinetics and thermodynamic exchanges between nanomaterials surfaces and the surfaces of biological components.[2] Some of these interactions may be transient, with proteins on a come-and-go

basis, while others are stable, with proteins getting "adsorbed" and forming a protein corona on the surface of nanoparticles.[3]

Proteins and organic substances increase the dissolution rates of nanoparticles through aqueous complexation and ligand-enhanced dissolution,[3] simultaneously, protein denaturation[4,5] and aggregation[6,7] have frequently been reported for proteins bound to inorganic nanoparticles, with the resulting biological consequences such as inflammation. Recently, various nanomaterials, like iron core-gold shell nanoparticle,[8] luminescent Au-Nanocluster,[9-11] MnO nanocrystals,[12] VO_2 nanocrystals,[13] europium hydroxide nanorods,[14] lanthanide-based nanocrystals,[15] iron oxide,[16] gold, graphene,[17] and quantum dots [18] etc., elicit an autophagic response and anticancer activity in the various cancer cell culture systems, is examined. Apoptotic signaling preeminence to activation of caspases,[19] which particularly cleave partial proteome substrates after aspartate residues, loss or gain of function, or loss of complex formation.[20] Cleavage of these substrates during apoptosis direct to the typical biochemical and morphological characteristics, such as chromatin condensation, DNA fragmentation, cell shrinkage, and membrane blebbing.[21]

Most recently, ligand functionalized Mn_3O_4 NPs have been investigated extensively as a therapeutic agent for rapid treatment of hyperbilirubinemia, through direct removal of bilirubin (BR) from blood, both *in vitro* and *in vivo*.[22,23] Moreover, surface modification induced origin of novel optical, magnetic and catalytic properties have also been studied recently.[24]

Here we explore the effects of surface chemistry modulation of Mn_3O_4 nanoparticles through fractional removal of surface ligands and altering the surface oxidation states of the metal ions, without hampering the overall identity and morphology of the nanocrystals. We define how this surface property variation modify the fundamental forces at the nano-bio interface and govern Beclin-1 dependent signal transduction to tune autophagy and subsequent enhancement of apoptosis. Beclin-1 recently identified as a novel Bcl-2 homology

domain-3 (BH3)-only member of the B-cell lymphoma-2 (Bcl- 2) family, it reflects Bcl-2 homology-3 (BH3) domain that mediates its interaction with the antiapoptotic proteins Bcl-2.[25] Binding of Beclin-1 to Bcl-2 inhibits the autophagic function of Beclin-1,[26] exposing that Beclin-1 might endeavor the convergence between autophagy and apoptotic cell death.[27] The classical hypothesis contributes caspase mediated cleavage of Beclin-1, inactivates Beclin-1 induced autophagy and enhances apoptosis,[28] in this study we aim to illustrate the crosstalk between these pathways and explore the fate of the autophagic proteins Beclin-1 and PI3KC3, during caspase mediated cleavage of autophagic proteins and tuning autophagy enhanced apoptosis in the context of surface modification of Mn_3O_4 nanoparticles. Moreover, the identification of another independent nature of Beclin-1 cleavage/splice pattern dependent on the NPs surface property, may interlink between autophagic tuning & enhancement of apoptosis. Our data clearly demonstrate the interplay between autophagy and apoptosis, as the nano-surface chemistry regulated caspase activation simultaneously tune autophagy and prolonged enhancement of apoptosis, which may in turn will help to adjust the drug delivery approach for anticancer therapy by linking up between nanomaterials surface chemistry with the cellular mechanism of cancer cells.

2. Experimental Section

Establishment and Cell culture of EGFP-LC3/HeLa/HUVEC cells

The reagents for cell culture were purchased from Gibco (Carlsbad, CA). The cells used in our experiment were grown continuously as monolayer at 37°C and 5% CO_2 in Dulbecco's Modified Eagle's medium (DMEM) and supplemented with 10% FBS. HeLa and HUVEC cells were transfected with pEGFP-LC3 plasmid using Lipofectamine 2000 and following the guidance of manufacturer's protocol, for over expression of EGFP-LC3 stably into cells. The cells were transferred to a new plate after 24 hours of transfection and underwent selection in DMEM medium containing 0.6 mg ml^{-1} of G418 (Promega, Madison,

WI, USA). Cell colonies exhibiting strong green fluorescence were observed and selected under a fluorescence microscope after 10 days of post-transfection and expansion.

GFP–LC3 dot formation and vacuolization

GFP–LC3 dot formation and vacuolization were observed under fluorescent microscopy in GFP–LC3/HeLa cells. Counting about 500 cells, GFP–LC3 dot formation was quantified and expressed ratio metrically where the number of cells with green fluorescence and cells with at least five GFP–LC3 dots were taken into account. Vacuolization was similarly quantified by identifying large cytosolic vacuole by counting 500 cells.

Synthesis and surface modification of Mn_3O_4 NPs

Mn_3O_4 NPs were synthesized following an ultrasonic assisted approach using 2-aminoethanol (2AE) as both solvent and complexing agent for the metal precursor, and without any additional surfactants or templates.[29] After synthesis of Mn_3O_4 NPs, the resulting suspension was centrifuged at 3000 rpm for 5 min. To wash the residual 2AE, the precipitate was washed three times with excess absolute ethanol. After centrifugation at 3000 rpm for 20 min, and drying at 70 ^{o}C for 30 min, a dark brown powder of Mn_3O_4 NPs was obtained. For partial surface oxidation of the NPs and fractional removal of the covalently attached 2AE ligands, as prepared Mn_3O_4 NPs were thermally annealed in a muffle furnace under atmospheric conditions at 350 ^{o}C for 1 hr.

Autophagic Marker Dye Staining

HeLa-LC3 cells, after Mn_3O_4 & Mn_3O_4 (A) NPs treatment, were stained for 15 minutes with 10 μM monodansylcadaverine (MDC) or 75 nM LysoTracker Red. After two times washing with PBS, cells were observed under fluorescence microscopy (Olympus IX71).

Western Blotting Analysis

Briefly, cells were cultured in 24-well plates to approximately 80% of confluence and treated with various compounds. After harvesting via trypsinization at the indicated times, cell

pellets were resuspended with the lysis buffer (0.5% Nonidet P-40/10 mM Tris-HCl, pH 7.5/100 mM NaCl) and supplemented with a protease inhibitor cocktail on ice. An equal volume of 2× sodium dodecyl sulfate (SDS) sample loading buffer (100 mM Tris-HCl, pH 6.8, 2% β -mercaptoethanol, 4% SDS, 20% glycerol, and 0.02% Bromphenol blue) was added, followed by boiling for 10–15 minutes. Proteins were separated on a 12%–15% SDS-polyacrylamide gel electrophoresis (SDS-PAGE) gel and transferred to nitrocellulose membrane (GE Healthcare Life Sciences). After blocking with Tris-buffered saline (TBS) containing 0.1% polyoxyethylene(20) sorbitan monolaurate (Tween-20) and 5% nonfat dry milk, the nitrocellulose membrane was incubated overnight at 4° C with a primary antibody at an appropriate dilution (1:2000-1:1000), extensively washed more than five times for 10 minutes each with TBST (TBS containing 0.1% Tween-20), incubated with HRP-conjugated secondary antibody (1:10000 dilution) for 1 hour at RT, extensively washed and finally visualized using an ECL kit.

Electron microscopy for observation of autophagosome

HeLa cells were grown in 24-well plates and treated with Mn_3O_4 and Mn_3O_4 (A) NPs for 24 hrs. Then cells were harvested, and fixed in suspension with 4% glutaraldehyde in 0.1 M calcodyate buffer (pH 7.3) and reserve overnight at 4°C, and then post-fixed for 1 hour at room temperature in 2% osmium tetraoxide in 0.1 M cacodylate. Cells were embedded in epoxy resin after dehydration by graded series of ethanol. Finally the sliced ultrathin sections of the cell were stained with uranyl acetate and lead citrate and examined under a transmission electron microscope (JEOL-1230, Japan).

Cell viability assay

To assess the cell viability MTT was used. In brief, at a density of approximately 10,000 cells per well, HeLa cells were grown in 96-well plates. After incubation of 20 hrs at 37°C and 5% CO_2 in Dulbecco's Modified Eagle's Medium (DMEM) supplement with 10% FBS, then cell were treated by Mn_3O_4 and Mn_3O_4 (A) NPs for 24 hrs and then MTT (thiazoyl

blue tetrazolium bromide; T0793-500MG, Bio Basic) was added to the growing cultures at a final concentration of 0.5 mg/mL and incubated for 4 h at 37°C. Then the media was removed out and formazan crystals were completely dissolved into 100 mL of dimethyl sulfoxide (DMSO). Finally the absorbance at 570 nm was measured with a spectrophotometer (Elx800, BioTek, Winooski, VT, USA). All the values were recorded triplicate & untreated cell were regarded as a control.

Apoptosis assay

Apoptosis assay ware performed with the ANXA5/Annexin V-FITC Apoptosis Detection Kit (Beyotime, C1062). First cells were collected from 6-well plates and two times washed with PBS followed by resuspension into 195 µL of binding buffer. At room temperature under dark condition cells were incubated for 10 min after addition of 5 µL of ANXA5-FITC stock solution. The cells were resuspended in 190 µL of binding buffer after low centrifugation. Finally the cells were immediately analyzed by FACS after addition of 10 µL propidium iodide (PI). In each samples approximately 3×10^4 cells were analyzed.

Plasmids & Transfection

The cDNA encoding human Beclin-1 was amplified by reverse transcription PCR from a HeLa cDNA library using primers 5'-ATAAGAATGCGGCCGCTATGGAAGGGT GACGTCCAACAAC-3' and 5'-TGCGGTCGACTCATTTGTTATAAAATTGTGAGGA CACC-3'. The amplified product was cloned in the pGFP-C1 vector in frame was constructed by inserting a EcoR1–Sal1 fragment containing human Beclin-1. Lentiviral-compatible shRNAs against Beclin-1 was set up using pLKO.1 puro vector (RMM4431-101259746, sense: ACAGGAGCTGGAAGATGTGGAA; RHS4430-98520944, sense: AGCCAATAAGATGGGTCTGAAA). Proper construction of all the plasmids was confirmed by DNA sequencing. All plasmid were transfected with Lipofectamine 2000 according to the manufacturer's protocol.

Transmission electron microscopy (TEM)

Mn_3O_4 and Mn_3O_4 (A) TEM images were taken using a JEOL JEM-2100F Transmission Electron Microscope at 200 kV. For cell TEM, HeLa cells, after the various treatments, were fixed in situ with 2.5% glutaraldehyde in cacodylate buffer (pH 7.4) for 60 minutes at 4°C, postfixed with 2% osmium tetroxide at room temperature for 60 min, dehydrated with a graded series of ethanol, and then embedded in epoxy resin (Epon 812). Areas containing cells were block mounted and cut into ultrathin sections. After staining with uranyl acetate and lead citrate, the sections were examined with a transmission electron microscope (JEOL-1230, JEOL, Japan).

Statistical analysis

All data were expressed as mean ± s.e.m. and analyzed by two-tailed Student's t-tests with a minimum n=3. P-values of less than 0.05 were considered significant.

3. Results and Discussion

Surface chemistry modulation of Mn_3O_4 NPs by surface oxidation and partial ligand removal

Mn_3O_4 NPs were synthesized using 2-aminoethanol (2AE) as both solvent and complexing agent, and the average size of the as-synthesized NPs were 8.25 nm (Supplementary Figure. S1). Since, $Mn^{2+/3+}$ centers in Mn_3O_4 has strong bonding affinity for -NH_2/-OH functional groups of 2AE, to estimate the exact amount of covalently bonded 2AE molecules surrounding each NPs after washing and drying steps, we have performed thermogravimetric (TG) and differential thermal analysis (DTA) of the as prepared Mn_3O_4 NPs. Figure 1b shows the weight loss of as prepared NPs upon heating to 600 °C. As evident from thermal curves, uncoordinated water molecules were detected associated with the NPs within temperature range of 50–100 °C, contributed to the weight loss of ~1.8% and DTA endothermic signal at ~102.3 °C. The broad exothermic major weight loss (6.28%) within 100-500 °C regions could be attributed to the decomposition of 2AE.[30,31] Based on the molecular weight of 2AE, the observed mass loss corresponds to 1.047 mM of 2AE per gram

- 8 -

of Mn_3O_4 NPs. Moreover, from weight loss and crystal structure of the NPs, it is revealed that each as-synthesized Mn_3O_4 NP is covered with approximately 1043 number of 2AE molecules.[32] At 350 ^{o}C, 75.15% of the 2AE molecules are removed from the NPs surface and almost 259 2EA molecules are still attached with each Mn_3O_4 NPs. The signature of 2AE (black line) in the FTIR (Figure. 1c) spectrum of as-synthesized Mn_3O_4 NPs clearly confirms the presence of 2AE molecules on the NPs surface. Moreover, significant shift and broadening of 2AE absorption peaks at 1071 (C–O stretching vibration), 1487 and 1575 (coupling of in-plane bending of NH groups and C–N stretching, respectively), 2876 and 2944 (asymmetric CH_2 and the symmetric CH_2 stretching, respectively) and 3383 cm^{-1} (asymmetric stretching of NH_2 groups) [29,33] indicates the covalent conjugation of 2AE molecules with the Mn^{2+}/Mn^{3+} centers on the NPs surface. The presence of 2AE molecules on the NPs surface at 350 ^{o}C is further corroborated from FTIR study (Figure. 1c) of the as-synthesized Mn_3O_4 NPs thermally annealed at 350 ^{o}C for 1 hr. The annealed sample is termed as Mn_3O_4 (A) hereafter. As shown in the spectrum of Mn_3O_4 (A), the peaks at 1442, 1628, 2854 and 3419 cm^{-1} are further broadened and slightly shifted towards higher energy, indicating stronger bonding interaction of the remaining 2AE molecules with the surface $Mn^{2+/3+}$ metal ions, due to high temperature annealing. Thermal annealing also affects the characteristic stretching vibrations modes of Mn–O (625 cm^{-1}) and Mn–O–Mn (516 cm^{-1})[34,35] bonds of as-synthesized Mn_3O_4 NPs, reflecting from the high energy shift and substantial broadening of the corresponding peaks. For Mn_3O_4 (A), Raman study (Supplementary Figure. S3) also shows a significant perturbation in the characteristic Mn–O breathing vibration of tetrahedrally coordinated divalent Mn ions[36], with a significant shift and broadening of the main Raman peak of Mn_3O_4 NPs at 656 cm^{-1}. Although, a significant alteration in the surface characteristic of the NPs is evident from FTIR and Raman measurements, however, as shown in XRD pattern (Supplementary Figure. S2) of Mn_3O_4 (A), there is no significant change in the crystal structure of the NPs, except slight improvement in the crystallinity (evident from little

increase in intensity of the diffraction peaks). From high resolution TEM (HR-TEM) study (Figure. 1d and 1e) it is reveals that the diameter of Mn_3O_4 NPs remains almost same (~8 nm) for both Mn_3O_4 and Mn_3O_4 (A) NPs. To get clear insight about the surface characteristics of NPs, X-ray photo-electron spectroscopic (XPS) analysis has been carried out for both Mn_3O_4 and Mn_3O_4 (A). XPS survey spectrum of Mn_3O_4 NPs (Supplementary Figure. S4a) indicates the presence of Mn, O, C, and N, with N and C derived from 2AE molecules bonded with the Mn_3O_4 NPs. Figure S4b shows the high-resolution XPS spectra in Mn 2p core levels. The energy spacing due to spin-orbit splitting between the Mn $2p_{3/2}$ and Mn $2p_{1/2}$ states has been found to be 11.7 and 11.5 eV for Mn_3O_4 and Mn_3O_4 (A), respectively. In Mn $2p_{3/2}$ spectrum of Mn_3O_4, the peak at a binding energy of 640.7 eV is attributed to the +2 oxidation state of Mn, however, in Mn_3O_4 (A) the peak is observed at 641.1 eV, which is in agreement with +3 oxidation state of Mn.[37] Thus, for Mn_3O_4 NPs, nanosurface is dominated by +2 state of Mn, whereas, +3 state of Mn predominates in case of Mn_3O_4 (A). The O 1s peaks in Mn_3O_4 NPs (in Figure. S4c) at 529.5 and 531.1 eV are due to lattice oxygen (O^{2-}) associated with Mn and surface oxygen associated with hydroxyl ions (due to the presence of 2EA), respectively. [38,39] In case of Mn_3O_4 (A), little shift in the peak corresponding to lattice oxygen indicates a change in their coordination behavior, and bond weakening of the hydroxyl ions with the NPs surface is also detected due to peak shift of the corresponding bond towards higher energy. [40] So, from XPS study it is evident that, upon thermal annealing, NPs surface changes from Mn^{2+} rich phase to Mn^{3+} rich phase, along with dissociation of the covalently bonded 2AE molecules from the NPs surface. Figure 1a schematically shows the surface modification of Mn_3O_4 NPs. We intended to investigate the biological advantage of this surface chemistry modulation induced by partial removal of the surface ligands and alteration of surface oxidation states of the metal ions in the nanoparticle surface.

Establishment of autophagy induction by Mn_3O_4 NPs through enhancing autophagosome formation and sanction of autophagic tunning by Mn_3O_4 (A) NPs

We next assessed the impact of surface modified Mn_3O_4 NPs on autophagy induction activity indicated by a novel autophagy marker, LC3 conversion, in HeLa cell line treated with Mn_3O_4, Mn_3O_4 (A) & m-TOR-independent autophagic inducer, trehalose. Among the hallmarks to monitor the autophagic process, MAP1-LC3 (LC3) has so far been the best marker protein for autophagosomes.[41] Our result reveals (Fig. 2a) an increase level of LC3-II formation (16 kDa),[42] upon treatment with Mn_3O_4 and Mn_3O_4 (A) NPs, and most interestingly Mn_3O_4 (A) NPs shows higher LC3 conversion than Mn_3O_4. However, we didn't find any comprehensive LC3 conversion phenomena under similar condition with Y_2O_3, Eu_2O_3 and Nd_2O_3 NPs induction into HeLa cells (Supplementary Fig. S6). We have found that the best hallmark of autophagy indicator, LC3, converted from LC3-I to the membrane-bound form LC3-II dramatically, indicating that Mn_3O_4 (A) NPs induced more-powerful autophagy than Mn_3O_4. Moreover, we have checked if 2AE ligand itself can be effective in LC3 conversion, however, our results indicate that 2AE ligands alone is not effective unless it's bonded with Mn_3O_4 NPs surface (Supplementary Fig. S7).

To investigate the initial observation in details, we have assessed Mn_3O_4, Mn_3O_4 (A), Wortmannin, 3-methyl adenine (3- MA) and co-treatment of wortmannin /3-MA with Mn_3O_4/ Mn_3O_4 (A) to identify GFP–LC3 dot formation, an indication for negative regulation of genuine autophagy, in HeLa cell line established stably expressing green fluresent-protein-tagged microtubule-associated protein 1 light chain 3 (GFP–MAP1LC3), a fusion protein between Green Fluorescent Protein (GFP) and Microtubule-associated Light Chain 3 (LC3) protein. This protein randomly present in the cytoplasm, however appears as green puncatate dots upon induction of autophagy. Autophagy induction which was elicited by Mn_3O_4 and Mn_3O_4 (A), was significantly inhibited upon addition of 2.5 mM of 3-MA, a well-established autophagy inhibitor, and also similar phonomenon was observed for Wortmannin, a widely

used autophagy inhibitor that blocks the formation of autophagosomes through inhibition of class III phosphatidylinositol 3-kinase (PtdIns3K) pathway.[43] In both cases GFP-LC3 was evenly distributed in the untreated cells, a stable expressing GFP-LC3 in HeLa cell line. However, Mn_3O_4 (A) NPs treatment appeared as brighter punctate dots under fluorescence microscope than Mn_3O_4 NPs treated cells (Fig. 3), although in both NP cases punctate formation inhibitated by 3-MA & Wortmannin, as a result of GFP-LC3 conjugation to autophagosomes or cytosolic vaculation.[44] More assessmental confirmation obtained from the level of LC3-II, representing the endogenous LC3 protein that become attached to autophagosome membranes upon autophagy, was significantly elevated after Mn_3O_4 and Mn_3O_4 (A) NPs treatment. Our result clearly indicate that Mn_3O_4 (A) have higher efficiency for GFP punta formation than Mn_3O_4 NPs (Fig. 3). Moreover, our western blot data of Mn_3O_4, Mn_3O_4 (A) & with co-treated with autophagic inhibitor 3-MA also shows similar characteristics of LC3-II conversion (Fig. 2c).

Another important indicator for autophagic degradation is free GFP. To shed more light on this, we performed autophagic flux assays. When GFP-LC3 was delivered to a lysosome, the GFP part of the chimera was relatively resistant to hydrolysis. Therefore, the appearance of free GFP could be applied to monitor the breakdown of the cargo.[45] Chloroquine (CQ), a lysosomotropic compound, which blocks autophagic degradation by inhibiting vacuolar H^+ ATPase activity or by increasing the lysosomal pH causing autophagosome accumulation.[46] Flux analysis shows a much greater amount of the free GFP moiety in Mn_3O_4 (A) NPs treated cells than Mn_3O_4 NPs. Furthermore, the appearance of the free GFP moiety was suppressed efficiently on Mn_3O_4 (A) NPs and CQ co-treated cells by the saturating dose of CQ (Fig. 2e and Supplementary Fig. S8).[47] Interestingly, Mn_3O_4 and Mn_3O_4 (A) NPs treated cells were clearly suppressed GFP moiety wi cotreated with CQ. Mn_3O_4 and Mn_3O_4 (A) treatment also led to decrease in the level of p62 (SQSTM1/sequestosome1) protein, a cellular substrate for autophagy (Supplementary Fig. S9). These results strongly suggest that the observed higher

autophagosome accumulation by Mn_3O_4 (A) treatment was due to increased autophagic activity and not decreased autophagic turnover. Mn_3O_4 (A) exhibit significant measure of mitochondrial activity, by cell death promoting effect which abrogated by Mn_3O_4 NPs in HeLa cells at concentrations of over 100 μg ml^{-1}, and it's fail to established viability of the remaining cell population (Supplementary Fig. S10).

Collectively, these results demonstrate Mn_3O_4 (A) NPs have high efficiency than Mn_3O_4 NPs to induced autophagosome accumulation and autophagy induction, confirmed by EGFP-LC3 dots co-localization with the staining patterns with LysoTracker Red which stains acidic vesicles of the cells (Figure. 4) & live cell nuclear Hoechst staining. We have also observed that the number of vacuole-like structure formation in HeLa cells is larger when treated with Mn_3O_4 (A) NPs instead of Mn_3O_4 NPs (Fig. 5). As evident from the TEM images, Mn_3O_4 (A) NPs shows impressive ability to induce these vacuole-like features more higher than Mn_3O_4 NPs, and magnified TEM image clearly indicates the presence of autophagic vacuoles as white area, containing partially degraded cytoplasmic materials (Fig. 5b and 5c, down panel).

Mn_3O_4 (A) surface oxidized NPs accelerate autophagy by inhibiting caspase and Mn_3O_4 unable to accelerate autophagy by inhibiting apoptosis by caspase inhibitor

Our next finding assessed surface chemistry modulation of Mn_3O_4 NPs relational interlink between apoptosis and autophagy, apoptotic signaling activated by main proteases of caspases during caspase activation. We aimed to understand whether caspase mediated proteolysis can restrict the autophagy or not. We found that blocking of caspase activity by carbobenzoxy-valyl-analyl-aspartyl-[O-methyl]- fluoromethylketone (zVAD-fmk), a pan caspase inhibitor, prevented the processing of PI3KC3 and subsequently accelerate LC3 conversion (Fig. 6. a, b) and (Supplementary Fig. S11), indicating greater autophagy induction. Our results clearly indicate surface oxidized Mn_3O_4 (A) have high ability for caspase activation through generate cleave caspases. We found that the oxidized Mn_3O_4 (A)

surface can accelerate autophagy by blocking apoptosis through pan-caspase inhibitor. Considering this fact, a clear cross talk between autophagy and apoptosis in cells treated with oxidized Mn_3O_4 (A) NPs was revealed.

Caspase mediate cytoprotectative enhanced autophagy by surface oxidized Mn_3O_4 (A) NPs

Doxorubicin (Dox), a widely accepted chemotherapeutic agent that induce apoptosis via caspase 3 activation.[48] Here we employed Dox at non-cytotoxic concentration of 0.75 μg mL^{-1} co-trated with Mn_3O_4 and Mn_3O_4 (A) NPs along co-administrated with 3-MA and z-VAD to invistagate naturally tendent towards the speculation that the autophagy potency originating from those NPs. Notably, z-VAD-fmk can also alternatively decrease the level of autophagy by blocking caspase activation, although it failed to alter the accelerated autophagy level by Mn_3O_4 NPs co-administered with Dox. Interstingly Mn_3O_4 (A) explicitely increased the level of endogenus LC3-II while it co-administrated with Dox and z-VAD, which clearly shows surface oxidised Mn_3O_4 (A) have potency to inhibit caspase enrich to acclerate autophagy. Accordingly, 3-MA succeeded inhibiting the autophagy induced by combined treatment with Mn_3O_4 and Mn_3O_4 (A) NPs and Dox on HeLa cells. Appreantly without NPs the combined treatment of Dox and 3-MA on HeLa cells helpes to investigate us both Mn_3O_4 and Mn_3O_4 (A) have high potency of autophagy efficency which tuned by surface oxidation of NPs. These results strongly suggest that Mn_3O_4 NPs were unable to accelerate autophagy by blocking apoptosis where as Mn_3O_4 (A) have the ability to acclerate autophagy by induced cyto-protective autophagy, and thus would presumably decrease the efficacy of anti-cancer drugs such as DoX through blocking apoptosis (Fig. 7).

Beclin-1 protective Mn_3O_4 NPs surface modulation induced Beclin-1 distinguished cleavage/splices pattern

Our next investigation determined that Mn_3O_4 & Mn_3O_4 (A) NPs are able to cleave Beclin-1 by distinguished pattern (Fig. 8a), but are not essentially promoting apoptosis

through terminating autophagy. Here we found a novel phenomena, Mn_3O_4 induced autophagy & Mn_3O_4 (A) induced enhance autophagy leading to apoptosis may not concern the cleaving/splicing site of Beclin-1 for promoting apoptosis. Our western blot results showed that Beclin-1 was cleaved in a different pattern in cells treated with Mn_3O_4 and Mn_3O_4 (A), Beclin-1 was cleaved more at 58 kDa in case of Mn_3O_4 NP treated cells.

Considering this valuable fact, we studied Beclin-1 full length fusion protein transfected into HeLa cells, and observed that Beclin-1 cleaved into two major fragments, where the fragment of cleaved Beclin-1 remains at same position of 58 kDa and 37 kDa but the contrast of cleaving was higher for Mn_3O_4 NPs (Fig. 8c), also PARP & caspases were cleaved by Mn_3O_4 due to Beclin-1 over expression function, which strongly corroborate the role of NPs surface chemistry towards Beclin-1 dependent enhancement of autophagy (Supplementary Figure. S12, b) & apoptosis promotion. Combining the results of enhanced autophagy in Mn_3O_4 (A) NPs, we anticipate that this difference in Beclin-1 cleavage and the subsequent PI3K-C3 cleavage contributed to the difference in autophagy induction of these two NPs.

We also show that shRNA mediated stable knock down of Beclin-1 on HeLa & HUVEC cells were unable to initiate autophagy when treated with Mn_3O_4 or Mn_3O_4 (A) NPs. Our data illustrate that Mn_3O_4 (A) NPs were unable to accelerate autophagy tunning by GFP dot formation on HUVEC cells (Supplementary Fig. S13), and LC3 conversion (Fig. 8b). Together these results clearly demonstrate that Beclin-1 is directly responsible for the tunning of autophagy induction by Mn_3O_4 and/or Mn_3O_4 (A) NPs.

Mn_3O_4 (A) NPs provoked higher level of apoptosis than Mn_3O_4 NPs

We assessed apoptosis activation by monitoring the cleavage of poly (ADP-ribose) polymerase (PARP) at 89 kDa, a classical caspase-3 substrate, PARP caspase fragment were highly detected in HeLa cells co-treated with Mn_3O_4 (A) NPs. We have found that the cleavage of PI3KC3 at 50kDa is activated for Mn_3O_4 (A), in comparison with unmodified Mn_3O_4 NPs (Fig. 9a). We infer that surface chemistry variation in case of Mn_3O_4 (A) plays

the critical role in increasing PARP cleavage level, which is also correlated with the LC3 conversion level. Furthermore, the cleavage of PARP (Supplementary Fig. S12. b), an event downstream of caspase activation, is a biomarker of the end-stage of apoptosis.[27] Confirmation of these facts was observed when we evaluated apoptotic cell death efficiency of Mn_3O_4 and Mn_3O_4 (A) by ANXA5-FITC PtdIns assay of HeLa cells, where Dox were used as a positive control (Fig. 9b).

Bcl-2 family proteins have been associated with Beclin-1-BH3 domain. Bcl-2 homology (BH) domain (s) have been divided by Bcl-2 family proteins based on subgroups. Beclin-1 has a BH3 domain that binds to a hydrophobic groove in Bcl-2/Bcl-xL, so Bcl-2 family proteins also regulate apoptosis.[49] Here our study reveals that, BH3 domain released during beclin-1 cleavage, by Mn_3O_4 and Mn_3O_4 (A), initiates apoptotic nature by suppression of Bcl-2 (Fig. 9a).

4. Conclusions

In this work we demonstrate the feasibility of surface chemistry modulation to 'tune' the cell signaling and autophagy-inducing activity of Mn_3O_4 nanoparticles. We have modified the surface chemistry of Mn_3O_4 nanoparticles by partial oxidation of the surface Mn^{2+} ions and fractional removal of surface coordinated 2AE ligands, and systematically explored the possibility of controlling the autophagy induction. By analyzing autophagosome formation and autophagy-associated biomarkers, we have identified autophagosome formation ability of Mn_3O_4 NPs, and acceleration of autophagy contrast and subsequent enhancement of apoptosis by surface modified Mn_3O_4 (A) NPs. These findings demonstrate that potential pharmaceutical autophagy-apoptosis conflict modulators and biocompatible nanomaterials can be developed through nanoparticle surface modifications. Differences in surface chemistry allow Mn_3O_4 NPs to trigger autophagy through signaling pathways, demonstrating the flexibility and specificity of autophagy modulation by nanoparticles as a result of well-

defined interactions with specific molecular signaling pathways. Mn_3O_4 NPs induced LC3 conversion, GFP-LC3 dot formation, cargo breakdown from autophagy flux through free GFP, and identification of autophagosome formation through TEM of HeLa cells, were investigated to identify the signaling pathways. Moreover, in our study we shows that blocking caspase activity by pan-caspase inhibitor can accelerate autophagic induction by Mn_3O_4 (A) NPs, where as direct caspase activation not happens in case of Mn_3O_4 NPs.

We have observed that phenomena of Beclin-1 exclusive cleavage/splice, that could be a short noval varient of Beclin-1,[50] results in the subsequent formation of both the Beclin-1-PI3KC3 complex & its derivative, which are autophagic. BH3 domain of Beclin-1 subsequently interacts with Bcl-2 protein and act as anti-apoptotic feature. Our result shows that the novel cleavage/splice of Beclin-1 is not at all essential to terminate autophagy and apoptosis promotion, unless PI3KC3 initiate to cleave. Thus Beclin-1 cleavage dependent and Beclin-1 protective autophagy & enhance apoptosis signaling, depends particularly on Mn_3O_4 NPs surface chemistry, where Beclin-1 distinct cleavage/splice (different from other cleavage pattern) have significantly supporting to switch enhance apoptosis from autophagy via caspase activated PI3KC3 pathway (Supplementary Scheme. S1).

References

(1)   Ravikumar, B. Regulation of Mammalian Autophagy in Physiology and Pathophysiology. *Physiol. Rev.* **2010**, *90*, 1383.

(2)   Nel, A. E.; Madler, L.; Velegol, D.; Xia, T.; Hoek, E. M. V.; Somasundaran, P.; Klaessig, F.; Castranova, V.; Thompson, M. Understanding Biophysicochemical Interactions at the Nano-Bio Interface. *Nat. Mater.* **2009**, *8*, 543.

(3)   Xia, T.; Kovochich, M.; Liong, M.; Mädler, L.; Gilbert, B.; Shi, H.; Yeh, J. I.; Zink, J. I.; Nel, A. E. Comparison of the Mechanism of Toxicity of Zinc Oxide and Cerium Oxide Nanoparticles Based on Dissolution and Oxidative Stress Properties. *ACS Nano* **2008**, *2*, 2121.

(4)   Shen, J.-W.; Wu, T.; Wang, Q.; Kang, Y. Induced Stepwise Conformational Change of Human Serum Albumin on Carbon Nanotube Surfaces. *Biomaterials* **2008**, *29*, 3847.

(5)   Maoyong, S.; Guibin, J.; Junfa, Y.; Hailin, W. Inhibition of Polymerase Activity by Pristine Fullerene Nanoparticles can be Mitigated by Abundant Proteins. *Chem. Commun.* **2010**, *46*, 1404.

(6)   Vertegel, A. A.; Siegel, R. W.; Dordick, J. S. Silica Nanoparticle Size Influences the Structure and Enzymatic Activity of Adsorbed Lysozyme. *Langmuir* **2004**, *20*, 6800.

(7)   Sanpui, P.; Paul, A.; Chattopadhyay, A. Theranostic potential of gold nanoparticle-protein agglomerates. *Nanoscale* **2015**, *7*, 18411.

(8)   Ma, X.; Wu, Y.; Jin, S.; Tian, Y.; Zhang, X.; Zhao, Y.; Yu, L.; Liang, X.-J. Gold Nanoparticles Induce Autophagosome Accumulation through Size-Dependent Nanoparticle Uptake and Lysosome Impairment. *ACS Nano* **2011**, *5*, 8629.

(9)   Zhang, Q.; Yang, W. J.; Man, N.; Zheng, F.; Shen, Y.; Sun, K.; Y., L.; Wen, L. Autophagy-Mediated Chemosensitization in Cancer Cells by Fullerene C60 Nanocrystal. *Autophagy* **2009**, *5*, 1107.

(10)   Song, X.-R.; Goswami, N.; Yang, H.-H.; Xie, J. Functionalization of metal nanoclusters for biomedical applications. *Analyst* **2016**, *141*, 3126.

(11)   Zhang, X.-D.; Luo, Z.; Chen, J.; Shen, X.; Song, S.; Sun, Y.; Fan, S.; Fan, F.; Leong, D. T.; Xie, J. Ultrasmall Au10−12(SG)10−12 Nanomolecules for High Tumor Specificity and Cancer Radiotherapy. *Adv. Mater.* **2014**, *26*, 4565.

(12)   Lu, Y.; Zhang, L.; Li, J.; Su, Y.-D.; Liu, Y.; Xu, Y.-J.; Dong, L.; Gao, H.-L.; Lin, J.; Man, N.; Wei, P.-F.; Xu, W.-P.; Yu, S.-H.; Wen, L.-P. MnO Nanocrystals: A Platform for Integration of MRI and Genuine Autophagy Induction for Chemotherapy. *Adv. Funct. Mater.* **2013**, *23*, 1534.

(13)   Wei, Z.; Yanyan, M.; Yunjiao, Z.; Liang, L.; Jun, L.; James, Y. Y.; Yi, X.; Longping, W. Induction of Cyto-Protective Autophagy by Paramontroseite VO_2 Nanocrystals *Nanotechnology* **2013**, *24*, 165102.

(14)   Wei, P.-F.; Zhang, L.; Nethi, S. K.; Barui, A. K.; Lin, J.; Zhou, W.; Shen, Y.; Man, N.; Zhang, Y.-J.; Xu, J.; Patra, C. R.; Wen, L.-P. Accelerating the Clearance of Mutant Huntingtin Protein Aggregates Through Autophagy Induction by Europium Hydroxide Nanorods. *Biomaterials* **2014**, *35*, 899.

(15)   Zhang, Y.; Zheng, F.; Yang, T.; Zhou, W.; Liu, Y.; Man, N.; Zhang, L.; Jin, N.; Dou, Q.; Zhang, Y.; Li, Z.; Wen, L.-P. Tuning the Autophagy-Inducing Activity of Lanthanide-based Nanocrystals Through Specific Surface-Coating Peptides. *Nat. Mater.* **2012**, *11*, 817.

(16)   Khan, M. I.; Mohammad, A.; Patil, G.; Naqvi, S. A. H.; Chauhan, L. K. S.; Ahmad, I. Induction of ROS, Mitochondrial Damage and Autophagy in Lung Epithelial Cancer Cells by Iron Oxide Nanoparticles. *Biomaterials* **2012**, *33*, 1477.

(17)   Markovic, Z. M.; Ristic, B. Z.; Arsikin, K. M.; Klisic, D. G.; Harhaji-Trajkovic, L. M.; Todorovic-Markovic, B. M.; Kepic, D. P.; Kravic-Stevovic, T. K.; Jovanovic, S. P.; Milenkovic, M. M.; Milivojevic, D. D.; Bumbasirevic, V. Z.; Dramicanin, M. D.; Trajkovic, V. S. Graphene Quantum Dots as Autophagy-Inducing Photodynamic Agents. *Biomaterials* **2012**, *33*, 7084.

(18)   Seleverstov, O.; Zabirnyk, O.; Zscharnack, M.; Bulavina, L.; Nowicki, M.; Heinrich, J.-M.; Yezhelyev, M.; Emmrich, F.; O'Regan, R.; Bader, A. Quantum Dots for Human Mesenchymal Stem Cells Labeling. A Size-Dependent Autophagy Activation. *Nano Lett.* **2006**, *6*, 2826.

(19)   Riedl, S. J.; Shi, Y. Molecular Mechanisms of Caspase Regulation During Apoptosis. *Nat. Rev. Mol. Cell. Biol.* **2004**, *5*, 897.

(20)   Timmer, J. C.; Salvesen, G. S. Caspase substrates. *Cell Death Differ* **2006**, *14*, 66.

(21)   Luthi, A. U.; Martin, S. J. The CASBAH: A Searchable Database of Caspase Substrates. *Cell Death Differ* **2007**, *14*, 641.

(22)   Polley, N.; Saha, S.; Adhikari, A.; Banerjee, S.; Darbar, S.; Das, S.; Pal, S. K. Safe and symptomatic medicinal use of surface-functionalized Mn_3O_4 nanoparticles for hyperbilirubinemia treatment in mice. *Nanomedicine* **2015**, *10*, 2349.

(23)   Giri, A.; Goswami, N.; Sasmal, C.; Polley, N.; Majumdar, D.; Sarkar, S.; Bandyopadhyay, S. N.; Singha, A.; Pal, S. K. Unprecedented catalytic activity of Mn_3O_4 nanoparticles: potential lead of a sustainable therapeutic agent for hyperbilirubinemia. *RSC Advances* **2014**, *4*, 5075.

(24)   Giri, A.; Goswami, N.; Pal, M.; Zar Myint, M. T.; Al-Harthi, S.; Singha, A.; Ghosh, B.; Dutta, J.; Pal, S. K. Rational surface modification of Mn_3O_4 nanoparticles to induce multiple photoluminescence and room temperature ferromagnetism. *J. Mater. Chem. C* **2013**, *1*, 1885.

(25)   Maiuri, M. C.; Le Toumelin, G.; Criollo, A.; Rain, J. C.; Gautier, F.; Juin, P.; Tasdemir, E.; Pierron, G.; Troulinaki, K.; Tavernarakis, N.; Hickman, J. A.; Geneste, O.; Kroemer, G. Functional and Physical Interaction Between Bcl‑XL and a BH3‑like Domain in Beclin‑1. *The EMBO Journal* **2007**, *26*, 2527.

(26)   Oberstein, A.; Jeffrey, P. D.; Shi, Y. Crystal Structure of the Bcl-XL-Beclin 1 Peptide Complex: BECLIN 1 IS A NOVEL BH3-ONLY PROTEIN. *J. Biol. Chem.* **2007**, *282*, 13123.

(27)   Pattingre, S.; Tassa, A.; Qu, X.; Garuti, R.; Liang, X. H.; Mizushima, N.; Packer, M.; Schneider, M. D.; Levine, B. Bcl-2 Antiapoptotic Proteins Inhibit Beclin 1-Dependent Autophagy. *Cell* **2005**, *122*, 927.

(28)   Wirawan, E.; Vande Walle, L.; Kersse, K.; Cornelis, S.; Claerhout, S.; Vanoverberghe, I.; Roelandt, R.; De Rycke, R.; Verspurten, J.; Declercq, W.; Agostinis, P.; Vanden Berghe, T.; Lippens, S.; Vandenabeele, P. Caspase-Mediated Cleavage of Beclin-1 Inactivates Beclin-1-Induced Autophagy and Enhances Apoptosis by Promoting the Release of Proapoptotic Factors from Mitochondria. *Cell Death Dis.* **2010**, *1*, e18.

(29)   Lei, S.; Tang, K.; Fang, Z.; Zheng, H. Ultrasonic-Assisted Synthesis of Colloidal Mn_3O_4 Nanoparticles at Normal Temperature and Pressure. *Cryst. Growth Des.* **2006**, *6*, 1757.

(30)   Zardini, H. Z.; Davarpanah, M.; Shanbedi, M.; Amiri, A.; Maghrebi, M.; Ebrahimi, L. Microbial Toxicity of ethanolamines—Multiwalled Carbon Nanotubes. *J. Biomed. Mater. Res. Part A* **2014**, *102*, 1774.

(31)   Zarabadi-Poor, P.; Badiei, A.; Fahlman, B. D.; Arab, P.; Mohammadi Ziarani, G. One-Pot Synthesis of Ethanolamine-Modified Mesoporous Silica. *Ind. Eng. Chem. Res.* **2011**, *50*, 10036.

(32) Ofir, Y.; Samanta, B.; Arumugam, P.; Rotello, V. M. Controlled Fluorination of FePt Nanoparticles: Hydrophobic to Superhydrophobic Surfaces. *Adv. Mater.* **2007**, *19*, 4075.

(33) Yang, W.-d.; Liu, C.-y.; Zhang, Z.-y.; Liu, Y.; Nie, S.-d. One Step Synthesis of Uniform Organic Silver Ink Drawing Directly on Paper Substrates. *J. Mater. Chem.* **2012**, *22*, 23012.

(34) Huang, C.-C.; Khu, N.-H.; Yeh, C.-S. The Characteristics of Sub 10 nm Manganese Oxide T1 Contrast Agents of Different Nanostructured Morphologies. *Biomaterials* **2010**, *31*, 4073.

(35) Chen, H.; He, J. Facile Synthesis of Monodisperse Manganese Oxide Nanostructures and Their Application in Water Treatment. *J. Phys. Chem. C* **2008**, *112*, 17540.

(36) Buciuman, F.; Patcas, F.; Craciun, R.; R. T. Zahn, D. Vibrational Spectroscopy of Bulk and Supported Manganese Oxides. *Phys. Chem. Chem. Phys.* **1999**, *1*, 185.

(37) Nesbitt, H. W.; Banerjee, D. Interpretation of XPS Mn(2p) Spectra of Mn Oxyhydroxides and Constraints on the Mechanism of MnO_2 Precipitation. *Am. Mineral.* **1998**, *83*, 305.

(38) Shanmugam, S.; Gedanken, A. MnO Octahedral Nanocrystals and MnO@C Core−Shell Composites: Synthesis, Characterization, and Electrocatalytic Properties. *J. Phys. Chem. B* **2006**, *110*, 24486.

(39) Lee, J. W.; Hall, A. S.; Kim, J.-D.; Mallouk, T. E. A Facile and Template-Free Hydrothermal Synthesis of Mn3O4 Nanorods on Graphene Sheets for Supercapacitor Electrodes with Long Cycle Stability. *Chem. Mater.* **2012**, *24*, 1158.

(40) Some, S.; Kim, Y.; Hwang, E.; Yoo, H.; Lee, H. Binol Salt as a Completely Removable Graphene Surfactant. *Chem. Commun.* **2012**, *48*, 7732.

(41)   Klionsky, D. J. Guidelines for the use and Interpretation of Assays for Monitoring Autophagy in Higher Eukaryotes. *Autophagy* **2008**, *4*, 151.

(42)   Mizushima, N.; Yoshimori, T. How to Interpret LC3 Immunoblotting. *Autophagy* **2007**, *3*, 542.

(43)   Blommaart, E. F. C.; Krause, U.; Schellens, J. P. M.; Vreeling-Sindelárová, H.; Meijer, A. J. The Phosphatidylinositol 3-Kinase Inhibitors Wortmannin and LY294002 Inhibit Autophagy in Isolated Rat Hepatocytes. *Eur. J. Biochem.* **1997**, *243*, 240.

(44)   Mizushima, N.; Yoshimori, T.; Levine, B. Methods in Mammalian Autophagy Research. *Cell* **2010**, *140*, 313.

(45)   Chen, S.; Rehman, S. K.; Zhang, W.; Wen, A.; Yao, L.; Zhang, J. Autophagy is a Therapeutic Target in Anticancer Drug Resistance. *Biochimica et Biophysica Acta (BBA) - Reviews on Cancer* **2010**, *1806*, 220.

(46)   Ni, H. M.; Bockus, A.; Wozniak, A. L.; Jones, K.; Weinmann, S.; Yin, X. M.; Ding, W. X. Dissecting the Dynamic Turnover of GFP-LC3 in the Autolysosome. *Autophagy* **2011**, *7*, 188.

(47)   Chipuk, J. E.; Bouchier-Hayes, L.; Green, D. R. Mitochondrial Outer Membrane Permeabilization During Apoptosis: The Innocent by Stander Scenario. *Cell Death Differ* **2006**, *13*, 1396.

(48)   Du, C.; Fang, M.; Li, Y.; Li, L.; Wang, X. Smac, a Mitochondrial Protein that Promotes Cytochrome c–Dependent Caspase Activation by Eliminating IAP Inhibition. *Cell* **2000**, *102*, 33.

(49)   Oh, S.; E, X.; Ni, D.; Pirooz, S. D.; Lee, J. Y.; Lee, D.; Zhao, Z.; Lee, S.; Lee, H.; Ku, B.; Kowalik, T.; Martin, S. E.; Oh, B. H.; Jung, J. U.; Liang, C. Downregulation of Autophagy by Bcl-2 Promotes MCF7 Breast Cancer Cell Growth Independent of its Inhibition of Apoptosis. *Cell Death Differ* **2011**, *18*, 452.

(50)   Cheng, B.; Xu, A.; Qiao, M.; Wu, Q.; Wang, W.; Mei, Y.; Wu, M. BECN1s, a Short Splice Variant of BECN1, Functions in Mitophagy. *Autophagy* **2015**, *11*, 2048.
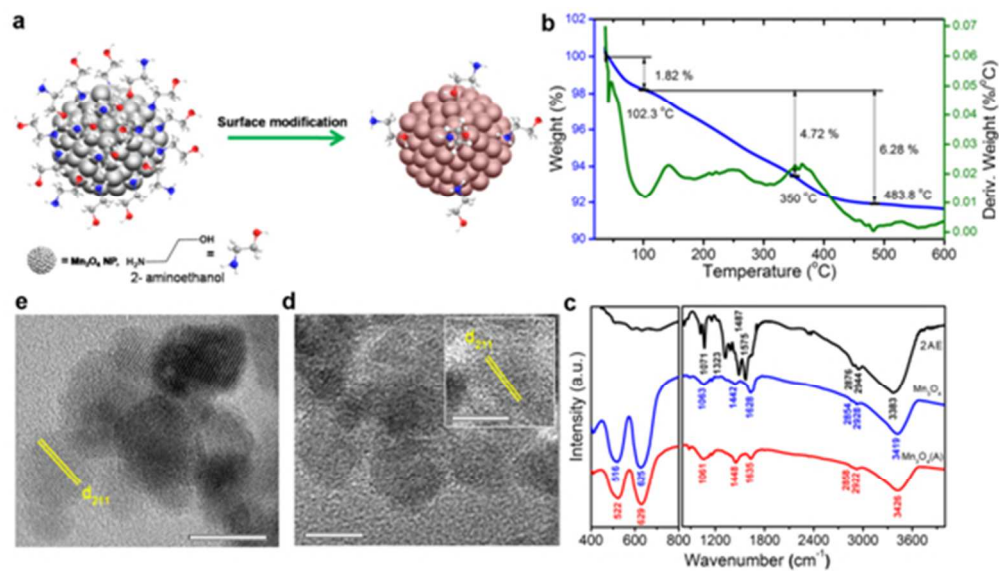
Figure1. Thermogravimetry identifies the optimum condition for surface modification, maintaining structural integrity of the Mn3O4 NPs. a, Schematically shows the surface modification of Mn3O4 NPs. b, TG/DTA thermal curves of the as prepared Mn3O4 NPs. c, FTIR spectra of 2AE, Mn3O4 and Mn3O4 (A) NPs recorded with a KBr pellet. d, TEM image of Mn3O4 NPs with a scale bar of 10 nm, inset shows high resolution TEM image of the same with scale bar of 5 nm. e, TEM image of Mn3O4 (A) NPs, scale bar is of 10 nm.

47x27mm (300 x 300 DPI)
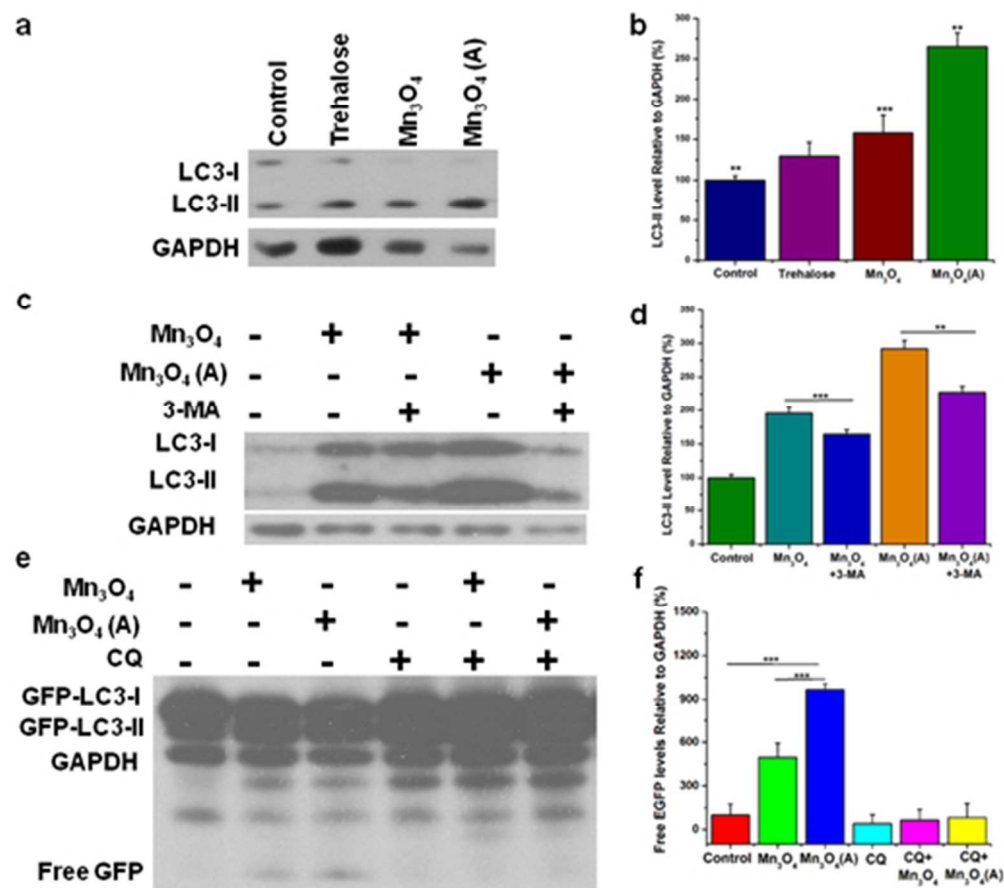
Figure 2. Tunning of autophagy induction elicited by Mn3O4 & Mn3O4 (A) NPs. a, HeLa cells were treated with PBS, trehalose (100 mM), Mn3O4 or Mn3O4 (A) (100μg mL-1) NPs for 24 hrs, endogenous LC3-II levels were detected by protein gel blotting with anti-LC3 antibodies, and in graph b, quantified by densitometry analysis relative to GAPDH. c, HeLa cells were treated with PBS, Mn3O4 or Mn3O4 (A) (100μg mL-1) NPs in presence or absence of 3-methyladenine (2.5 mM) for 24 hrs, LC3-II levels were detected by protein gel blotting with anti-LC3 antibodies, and in graph d, quantified by densitometry analysis relative to GAPDH. e, HeLa cells were treated with PBS, Mn3O4, Mn3O4 (A) and 50μM Chloroquine in presence or absence of Mn3O4 or Mn3O4 (A) (100μg mL-1) NPs for 24 hrs, free GFP levels were detected by protein gel blotting with anti GFP antibodies and in lower right graph f, quantified by densitometry analysis relative to GAPDH. Mean ± SEM, n=3. * P < 0.05, **P<0.01, *** P<0.001 for b, d, f.

43x39mm (300 x 300 DPI)
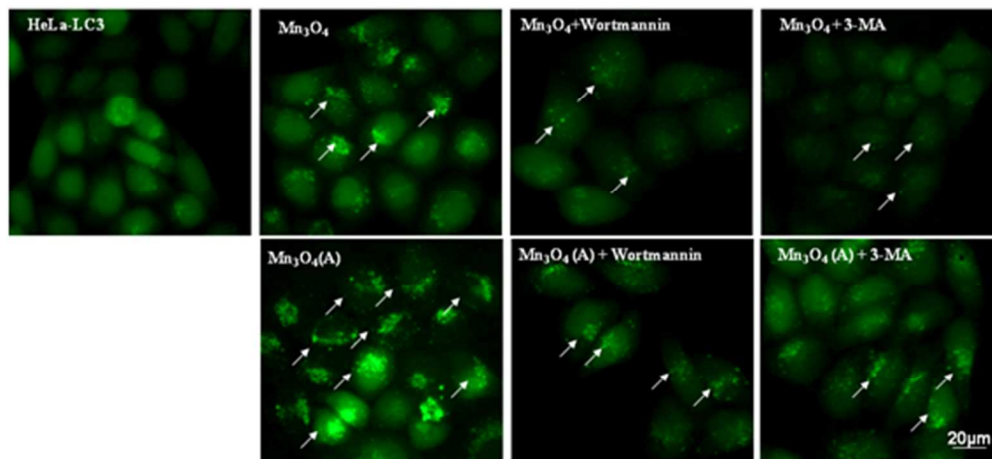
Figure 3. Fluorescence microscopy images of EGFP-LC3 dot formation inhibited by autophagic inhibitors in HeLa-LC3 cells when treated with PBS, Mn3O4 (100μg mL-1) and Mn3O4 (A) (100μg mL-1) added separately with Wortmannin (0.5 μM) or 3-methyladenine (2.5 mM) to EGFP-HeLa cells for 24 hrs incubation.
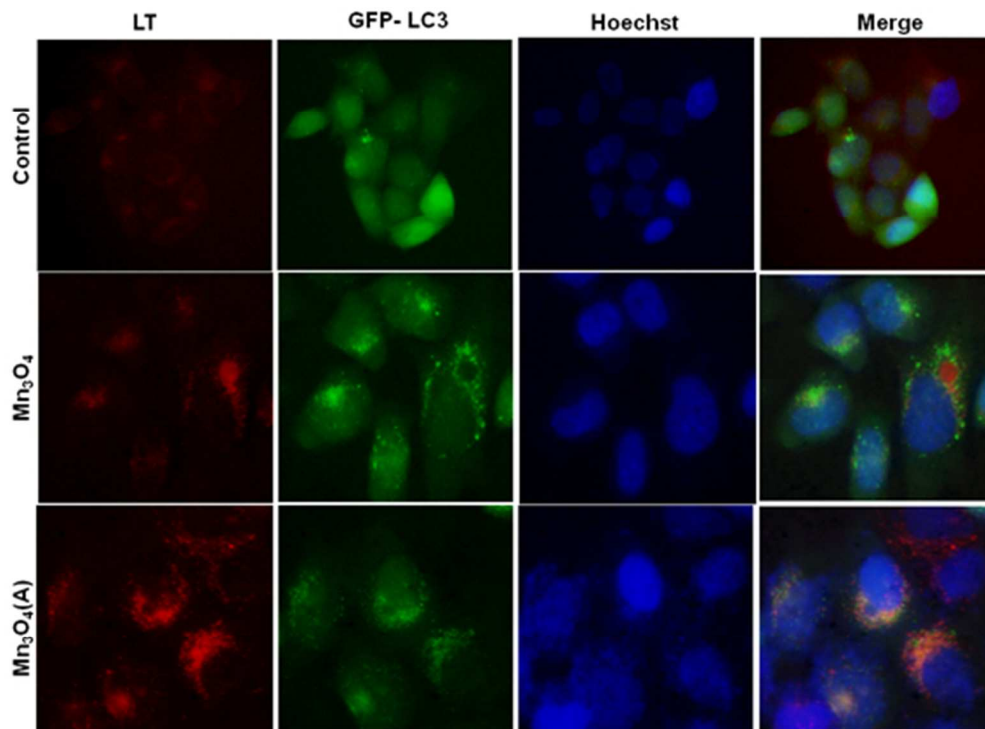
48x22mm (300 x 300 DPI)

Figure 4. Additional autophagic tunning features of Mn3O4 and Mn3O4 (A) NPs identified by increased autophagosome accumulation. Fluorescent co-localization between EGFP-LC3 dots and other autophagy-related markers: LysoTracker Red (LT) and Hoechst live cell stain in HeLa EGFP-LC3 cells treated with PBS, 100µg mL-1 Mn3O4 or Mn3O4 (A) NPs for 24 hrs.

48x35mm (300 x 300 DPI)
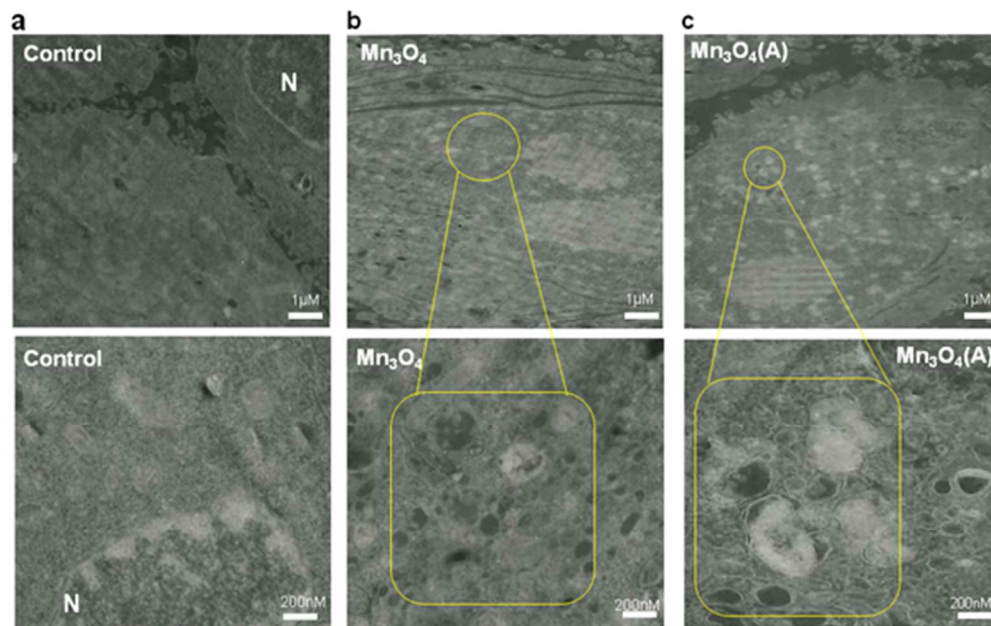
Figure 5. TEM image of HeLa cells were incubated with PBS (control), Mn3O4 (100µg mL-1) and Mn3O4 (A) (100µg mL-1) NPs for 24 h. The down panel is a high magnification image of the indicated portions in the corresponding images of the upper panel. Magnifying block indicates autophagosomes and autolysosomes. 'N' indicates the nucleus of the cell.
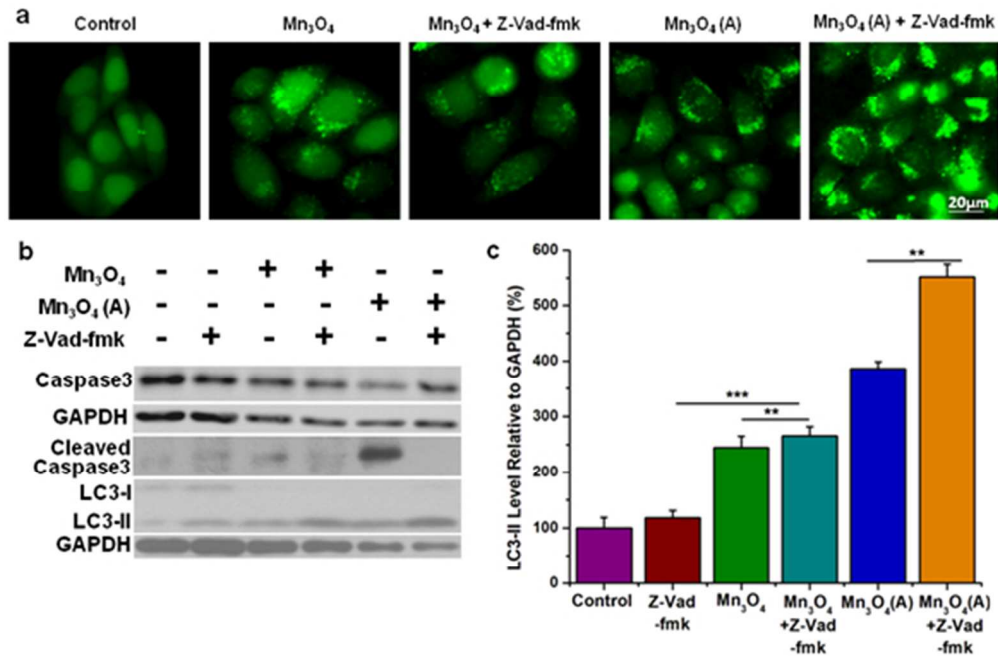
51x32mm (300 x 300 DPI)

Figure 6. Enhanced autophagy by caspase inhibition in HeLa cells treated with Mn3O4 (A) NPs. a, Fluorescence microscopy images of EGFP-LC3 dot formation of HeLa-LC3 cells treated with PBS, Mn3O4 (100μg mL-1), Mn3O4 plus z-VAD-fmk (20μM), Mn3O4 (A) (100μg mL-1) and Mn3O4 (A) plus z-VAD-fmk (20μ), for 24 hrs. b, Endogenous LC3, caspase 3 & cleave caspase levels were detected by protein gel blotting with anti-LC3 and anti-pro-caspase antibodies, and right side graph quantified the LC3-II level by densitometry analysis relative to GAPDH. Mean ± SEM, n=3. * P < 0.05, **P<0.01, *** P<0.001

49x32mm (300 x 300 DPI)

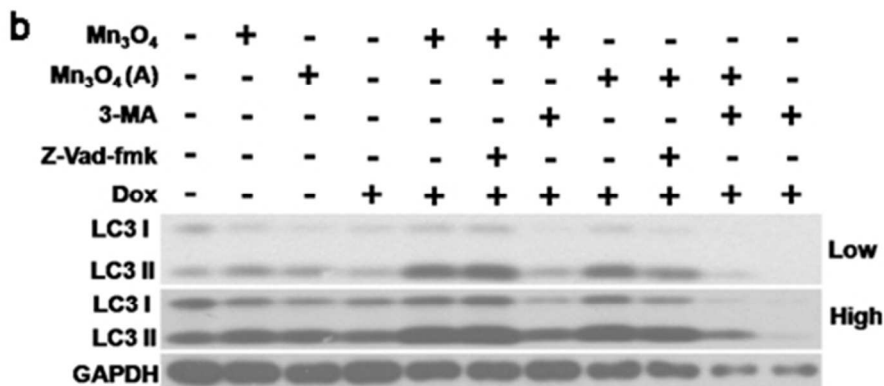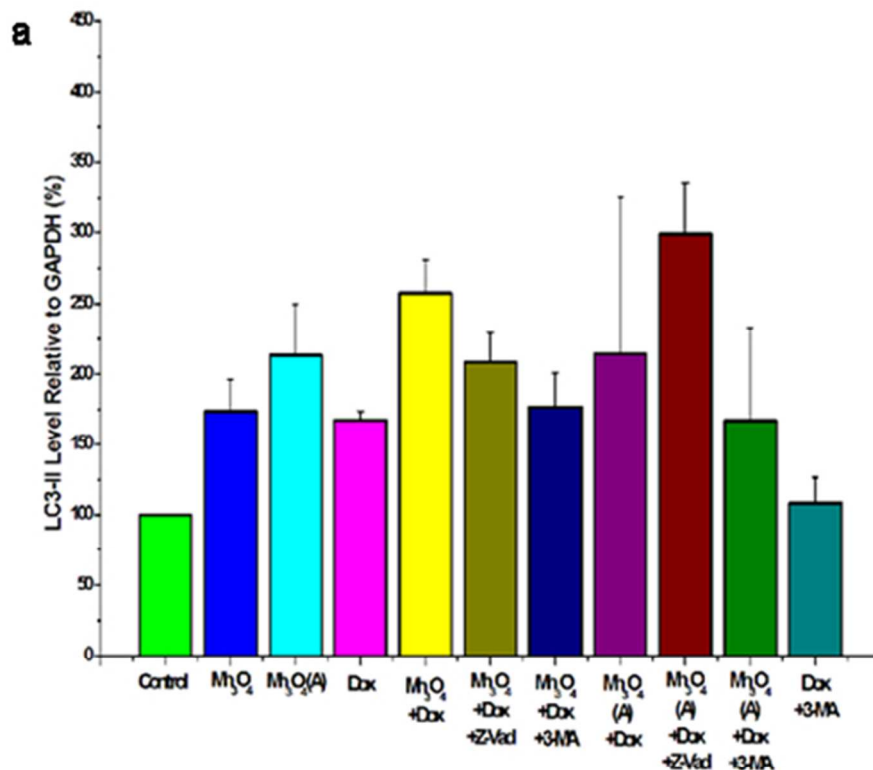Figure 7. Cytoprotective adjuvant autophagy enhances activity dependent upon Mn3O4 surface. HeLa cells were treated with PBS, Mn3O4 (100µg mL-1) and Mn3O4 (A) (100µg mL-1) NPs alone, Dox (0.75µg mL−1), Mn3O4 and Mn3O4 (A) NPs plus Dox or Mn3O4 and Mn3O4 (A) NPs plus Dox co-treated with 3-MA (2.5 mM) or z-VAD-fmk (20µM) for 24 hrs. a, upside graph quantified the LC3-II level by densitometry analysis relative to GAPDH. Mean ± SEM, n=3. b, Endogenous LC3-II levels were detected by protein gel blotting with anti-LC3 antibodies.
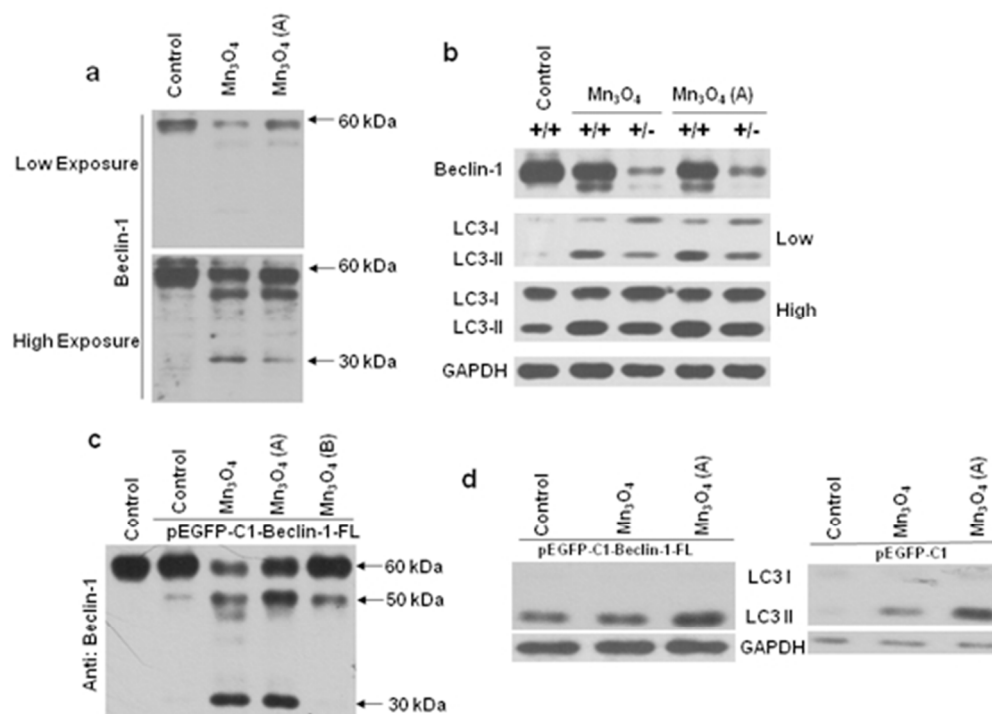
45x59mm (300 x 300 DPI)

Figure 8. Beclin-1 dependent Mn3O4 surface chemistry modulated distinguished cleave/splice of Beclin-1 protein. a, After treatment of HeLa cells with PBS, Mn3O4 and Mn3O4 (A) (100μg mL-1) NPs for 24 h, Beclin1 levels were detected by protein gel blotting. b, Endogenous LC3-II levels were detected by protein gel blotting with anti-LC3 antibodies relative to GAPDH, when HeLa (+/+) wild type & Beclin-1 shRNA knockdown HeLa (+/-) cells were treated separately with PBS and Mn3O4 or Mn3O4 (A) (100μg mL-1) NPs for 24 h. c, PBS, Mn3O4 , Mn3O4 (A) and Mn3O4 (B) (100μg mL-1) NPs was treated in HeLa cells transfected with Beclin-1 fusion protein contain in pEGFPC1 overexpansion vector for 24h, endogenous Beclin-1 cleavage pattern were detected by protein gel blotting with Beclin-1 antibodies. d, After 24 h incubation, endogenous LC3-II levels were detected by protein gel blotting by anti-LC3 in HeLa cells transfected with Beclin-1 fusion protein containing pEGFP-C1 overexpansion vector and pEGFP-C1 alone.

48x34mm (300 x 300 DPI)

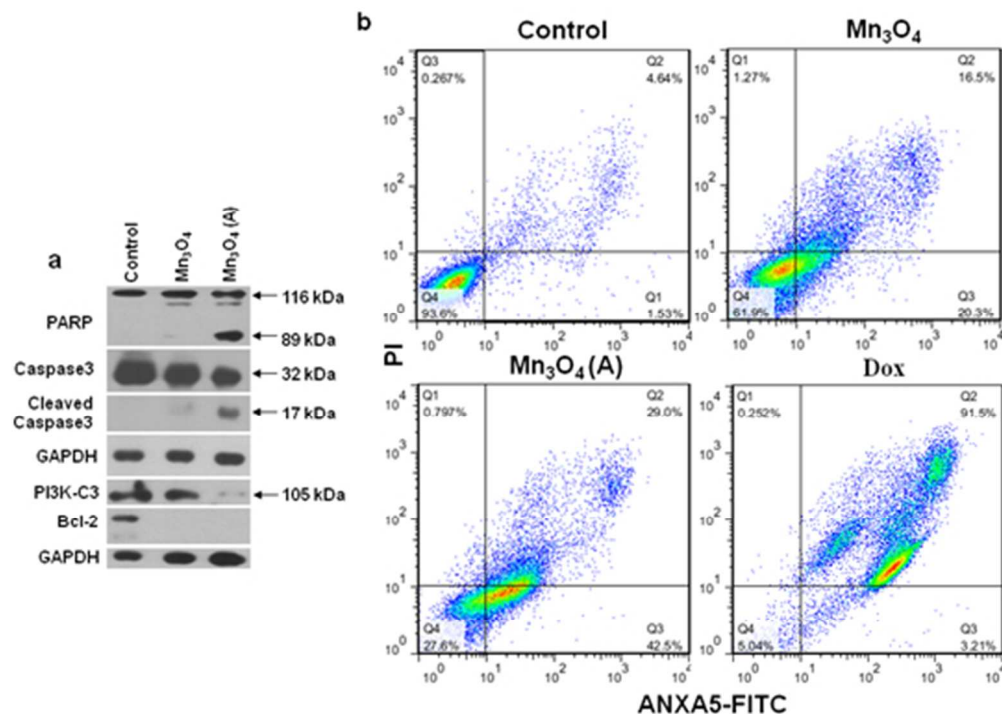Figure 9. Mn3O4 (A) NPs induce higher level of apoptosis than Mn3O4 NPs. a, After treatment of HeLa cells with PBS, Mn3O4 (100µg mL-1) and Mn3O4 (A) (100µg mL-1) NPs for 24 h, endogenous PARP, caspase 3, cleave caspase, Bcl-2 & PI3K-C3 levels were detected by protein gel blotting with PARP, procaspase, Bcl-2 & PI3K-C3 antibodies relative to GAPDH. b, ANXA5-FITC PtdIns assay of HeLa cells treated with PBS, Mn3O4 or Mn3O4 (A) (100µg mL-1) NPs & Dox (0.75µg mL−1) for 24 h, showing relative percentage of live (Q4 quadrant), early apoptotic (Q3 quadrant), and late apoptotic and necrotic (Q2 & Q1 quadrant) cells.

45x32mm (300 x 300 DPI)